# TUDelft

Delft University of Technology

Biomechanical evaluation of additively manufactured patient-specific mandibular cage implants designed with a semi-automated workflow
A cadaveric and retrospective case study

van Kootwijk, A.; Jonker, B. P.; Wolvius, E. B.; Saldivar, M. Cruz; Leeflang, M. A.; Zhou, J.; Tümer, N.; Mirzaali, M. J.; Zadpoor, A. A.

**Important note**
To cite this publication, please use the final published version (if applicable).
Please check the document version above.

# Biomechanical evaluation of additively manufactured patient-specific mandibular cage implants designed with a semi-automated workflow: A cadaveric and retrospective case study

A. van Kootwijk [a], B.P. Jonker [a], E.B. Wolvius [a], M. Cruz Saldivar [b], M.A. Leeflang [b], J. Zhou [b], N. Tümer [b,*], M.J. Mirzaali [b], A.A. Zadpoor [b]

[a] *Department of Oral and Maxillofacial Surgery, Erasmus University Medical Center, Doctor Molewaterplein 40, 3015 GE, Rotterdam, the Netherlands*
[b] *Department of Biomechanical Engineering, Faculty of Mechanical, Maritime and Materials Engineering, Delft University of Technology (TU Delft), Mekelweg 2, 2628 CD, Delft, the Netherlands*

## ABSTRACT

*Objective:* Mandibular reconstruction using patient-specific cage implants is a promising alternative to the vascularized free flap reconstruction for nonirradiated patients with adequate soft tissues, or for patients whose clinical condition is not conducive to microsurgical reconstruction. This study aimed to assess the biomechanical performance of 3D printed patient-specific cage implants designed with a semi-automated workflow in a combined cadaveric and retrospective case series study.

*Methods:* We designed cage implants for two human cadaveric mandibles using our previously developed design workflow. The biomechanical performance of the implants was assessed with the finite element analysis (FEA) and quasi-static biomechanical testing. Digital image correlation (DIC) was used to measure the full-field strains and validate the FE models by comparing the distribution of maximum principal strains within the bone. The retrospective study of a case series involved three patients, each of whom was treated with a cage implant of similar design. The biomechanical performance of these implants was evaluated using the experimentally validated FEA under the scenarios of both mandibular union and nonunion.

*Results:* No implant or screw failure was observed prior to contralateral bone fracture during the quasi-static testing of both cadaveric mandibles. The FEA and DIC strain contour plots indicated a strong linear correlation ($r = 0.92$) and a low standard error ($SE = 29.32 \ \mu\varepsilon$), with computational models yielding higher strain values by a factor of 2.7. The overall stresses acting on the case series' implants stayed well below the yield strength of additively manufactured (AM) commercially pure titanium, when simulated under highly strenuous chewing conditions. Simulating a full union between the graft and remnant mandible yielded a substantial reduction ($72.7 \pm 1.5 \%$) in local peak stresses within the implants as compared to a non-bonded graft.

*Conclusions:* This study shows the suitability of the developed semi-automated workflow in designing patient-specific cage implants with satisfactory mechanical functioning under demanding chewing conditions. The proposed workflow can aid clinical engineers in creating reconstruction systems and streamlining pre-surgical planning. Nevertheless, more research is still needed to evaluate the osteogenic potential of bone graft insertions.

Mandibular reconstruction is a common surgical intervention used to restore the continuity and function of the mandible, following tumor removal, osteomyelitis, trauma, or osteoradionecrosis (Kumar et al., 2016). The procedure is performed using a variety of techniques, typically including free tissue transfer and alloplastic reconstruction. The choice of the technique is determined by the specific characteristics of the defect, the patient's medical history, and the surgeon's expertise.

Advances in surgical techniques and additive manufacturing (AM) have enabled the design and manufacturing of patient-specific solutions, which are demonstrated to significantly improve the outcomes of mandibular reconstructions (Azarniya et al., 2019; Louvrier et al., 2017; Mirzaali et al., 2022, 2023; Oldhoff et al., 2021). However, such procedures remain complex and require a multidisciplinary team of specialists with specialized knowledge and skills to achieve optimal results.

Free flap reconstructions are associated with a high survival rate, but also have several drawbacks, such as limited availability of bone, morbidity of the donor site, prolonged operation time, necessity for specific surgical expertise, and the mechanical failure of osteosynthesis (Kakarala et al., 2018; Paré et al., 2019). Alternative techniques, such as reconstructions using a customized metallic cage implant with non-vascularized bone insertions, have shown promising results with minimal donor site morbidity, no additional surgical training or intra-operative bending of the plate, and excellent aesthetics (Kondo et al., 2015; Lee et al., 2018; Malekpour et al., 2014; Rachmiel et al., 2017; Yamashita et al., 2008; Zhou et al., 2010). We have recently developed a digital semi-automated workflow for designing patient-specific cage implants and developed finite element (FE) models to assess the biomechanical behavior of the implants (van Kootwijk et al., 2022). The design workflow aims to aid clinical engineers in creating reconstruction systems that can be used as a replacement or in conjunction with the free flap technique. Complementing this workflow with verified computational predictions of the patient-specific performance of the implant is expected to strengthen the decision-making process, thereby optimizing the biomechanical implant design and streamlining pre-surgical planning. The methods we reported were, however, at an early stage of development, having only undergone proof-of-concept testing on synthetic mandible models.

In this follow-up study, we have conducted a cadaveric study to evaluate the biomechanical safety of the cage implants and assess the efficacy of the semi-automated workflow proposed in (van Kootwijk et al., 2022) using actual human bone tissue. Two cage implants were designed for human cadaveric mandibles using this workflow. Both designs were processed, and 3D printed in compliance with the

European Medical Device Regulation (MDR). The biomechanical performance of the designs was then evaluated using finite element analysis (FEA) and quasi-static biomechanical testing. In addition, a retrospective case series was conducted to evaluate the biomechanical safety of the cage implants in a clinical setting. The implants investigated in the retrospective case series were similar in design to those used in the cadaveric study to enable a more straightforward comparison. The FE model of the cadaveric study was adapted to simulate physiological conditions and was customized to the clinical situation of each patient included in the case series. Together, these two types of studies are expected to enable a comprehensive assessment of the biomechanical safety and efficacy of the cage implants designed with the proposed semi-automated workflow, and help researchers identify any potential issues that would need to be addressed before the use of the design workflow and computational models in clinical practice.

## 1. Materials and methods

### 1.1. Cadaveric study

Two AnubiFiX™ embalmed (2% phenoxyethanol) human cadaveric mandibles were obtained from the Department of Anatomy and Neurosciences, Erasmus Medical Center (Erasmus MC), Rotterdam, The Netherlands, with the approval of the Medical Research Ethics Committee (MEC-2022-0200). The first cadaveric mandible (hereinafter CM1) was completely edentulous, whereas the second cadaveric mandible (hereinafter CM2) was partially dentulous with remaining incisors, canines, and first and second premolars. The morphometric measurements of each cadaveric mandible are presented in Fig. S1 and



**a.** Image processing    **b.** 3D model    **c.** Osteotomy planning    **d.** Segmental resection

**h.** Mesh implementation    **g.** Screw planning    **f.** Implant offset    **e.** Shape estimation

**i.** CM1 final design: virtual (left) and real (right)    **j.** CM2 final design: virtual (left) and real (right)
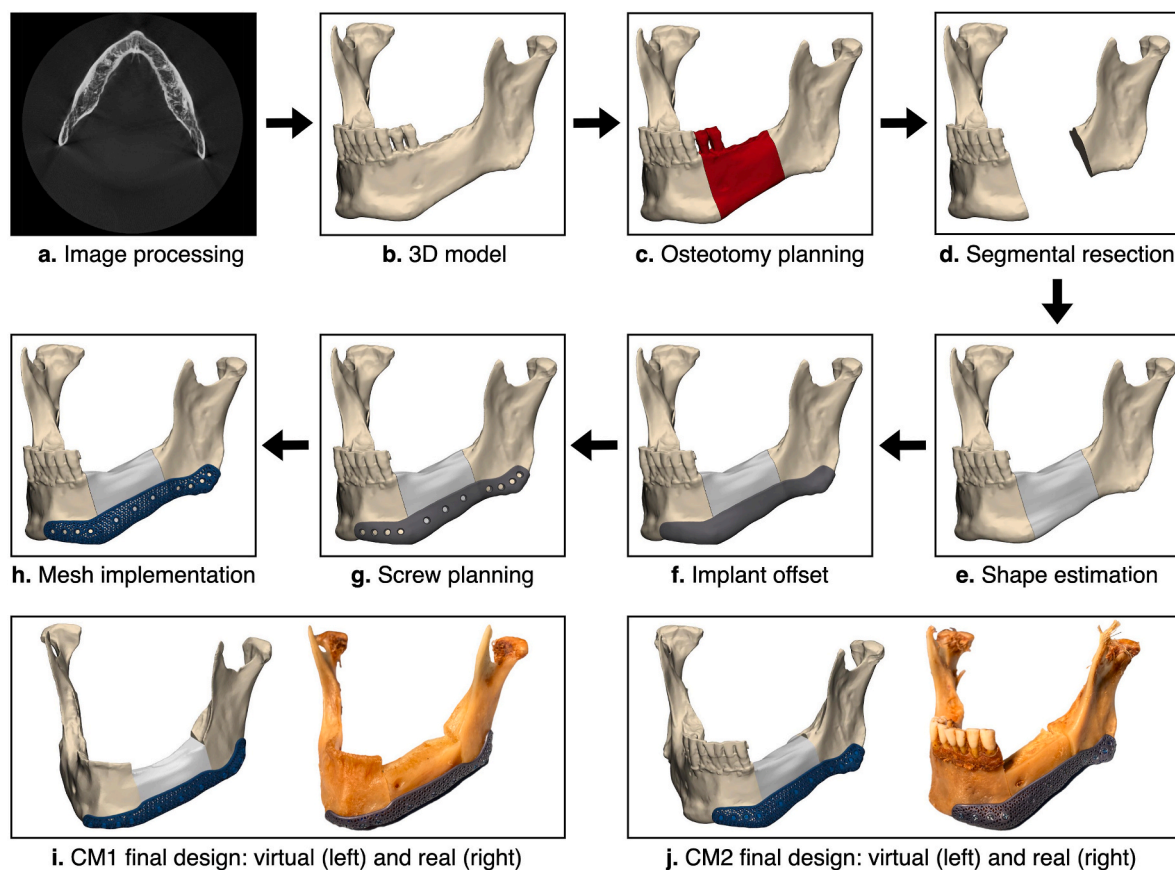
**Fig. 1.** The implant design workflow used for the CM2 case: (**a**) the segmentation of CT images; depicting an axial slice of the image stack, (**b**) the generation of the 3D model from segmented images, (**c**) the positioning of the two osteotomy planes, (**d**) the segmental resection, (**e**) the estimation of the missing bone segment, (**f**) the definition of outer shape and thickness of the implant, (**g**) the screw planning, and (**h**) the implementation of the porous mesh structure. The same workflow steps were used for the CM1 case. Final virtual design (left) and actual sample (right) of (**i**) CM1 and (**j**) CM2.

Table S1 (Supplementary document).

### 1.1.1. Implant design

The workflow proposed by Van Kootwijk et al. (van Kootwijk et al., 2022) (Fig. 1a–g) was used to design a solid implant for each of the cadaveric specimens. The cadaveric mandibles were scanned using a cone beam computed tomography (CBCT) scanner at a peak potential of 89 kVp and a slice thickness of 0.25 mm. The digital imaging and communications in medicine (DICOM) data was imported into Mimics Research 21.0 (Materialise, Belgium) where the image segmentation (Fig. 1a) and 3D model reconstruction (Fig. 1b) were carried out. The resulting mandible models were loaded in 3-matic 15.0 (Materialise, Belgium) where the osteotomy planning (Fig. 1c), segmental resection (Fig. 1d), the estimation of the resected bone segment (Fig. 1e), and implant design were carried out in collaboration with an experienced surgeon. A lateral defect measuring 4 cm in length was created in both specimens according to a previously described procedure (van Kootwijk et al., 2022). The shape of the implants was designed as a cage/tray, which would enable the insertion of bone grafts, and, ideally, rehabilitation with dental implants at a later stage. The implant thickness was set at 1.5 mm. An implant-bone clearance of 0.1 mm was used to prevent clamping (Fig. 1f). Eleven screw holes were planned for implant fixation with 2.0 mm self-tapping screws of which 4 screws were placed bicortically in each mandibular segment while 3 screws were placed monocortically in the mid-portion to secure the bone graft (Fig. 1g). The solid implant designs were processed by Materialise (Leuven, Belgium) for the implementation of the porous mesh structure and to ensure that the final designs followed the quality management system (QMS) for medical devices compliant with ISO 13485:2016. A porous mesh structure was implemented in the implant designs in the 3-matic software to decrease the stiffness of the implants and to promote osseointegration and angiogenesis (Fig. 1h). The porous mesh structure corresponded to the elementary pattern proposed by Barbas et al. (2012) and was characterized to have a theoretical porosity of 53% and pore sizes ranging between 860 μm and 1500 μm. All the implants used in this research were 3D printed with a Concept Laser M2 (GE Additive, Germany) by Materialise (Leuven, Belgium) from commercially pure titanium (CP-Ti; grade 2) using selective laser melting (SLM). After 3D printing, the implants underwent several post-processing procedures, such as heat treatment, support removal, anodization, various cleaning steps, rigorous quality control including optical scanning, and final packaging inside a clean room. The manufacturing and post-production processes were carried out in accordance with the QMS for both implants.

Surgical guides were designed and additively manufactured from Grey V4 commercial resin using a Formlabs Form 3 SLA printer (Somerville, MA, USA). They were then used for the cutting and predrilling procedures. Note that these guides were not intended for clinical use. Implant placement and sample preparation were performed by an experienced surgeon. The mandible specimens were cut along the osteotomy planes with an oscillating saw and a 1.45 mm drill bit was used to predrill the screw holes. The resected mandibular segment was placed in the cage implant, following minor shape refinements to substitute the virtually estimated bone graft (Fig. 1i and j).
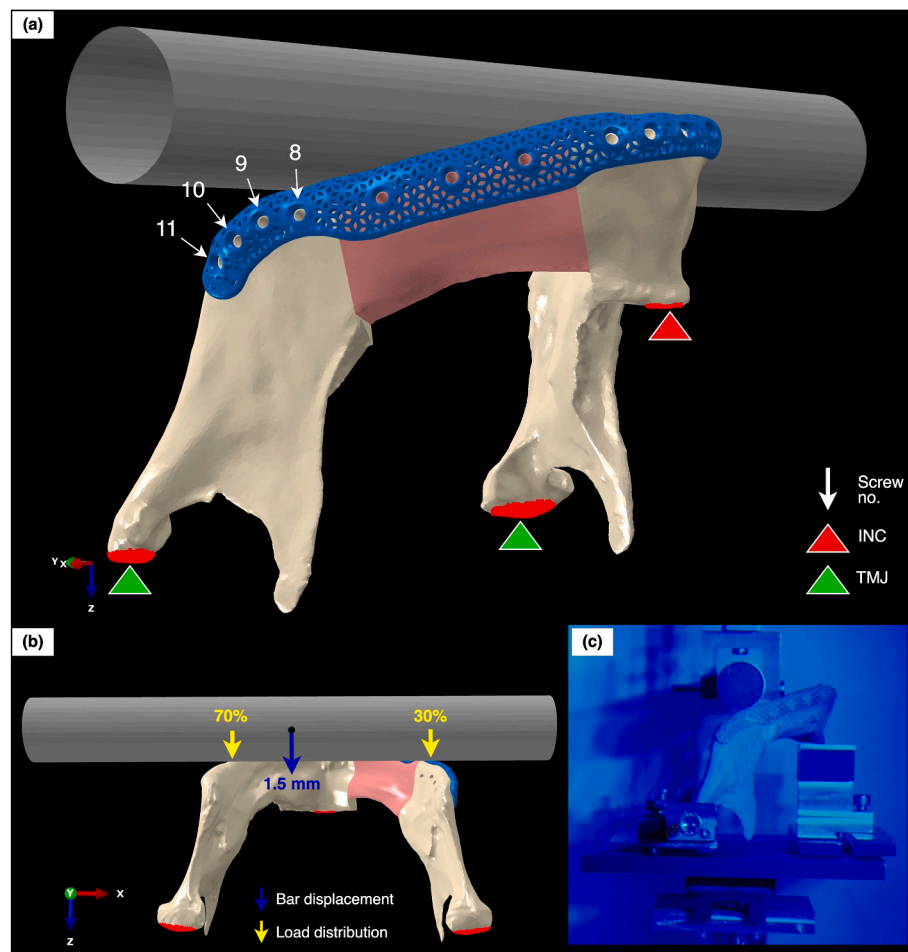


**Fig. 2.** (**a**) The boundary conditions and (**b**) displacements applied in the FE simulation of CM1. (**c**) The experimental test setup for CM1. A similar experimental setup was used for CM2.

### 1.1.2. Experimental testing

The biomechanical performance of the reconstructed CM1 and CM2 cadaveric mandibles was evaluated by means of quasi-static compressive testing on a mechanical testing machine (Lloyd Instruments LR5K) with a 5 kN load cell (Fig. 2c). The specimens were positioned upside-down in the testing setup proposed by Van Kootwijk et al. (van Kootwijk et al., 2022). A load was applied to the region of the mandibular angles using a rigid seesaw device. The loss of muscle force on the implanted side was accounted for by applying a distributed load, of which 70% and 30% were applied to the healthy and implanted sides of the mandible, respectively (Gateno et al., 2013; Schupp et al., 2007). All translational movements of both condyles were constrained, while allowing their rotational movements around the transverse horizontal axis. The incisal clenching (INC) task was carried out with a support structure that constrained the incisal region perpendicular to the occlusion plane. Quasi-static compressive loading was continuously applied to the mandibles at a displacement rate of 1 mm/min until failure occurred. The criteria for failure included mandible or implant fracture, screw-substrate interface failure, or vertical displacement of the loadcell exceeding 20 mm. Failure location, ultimate (failure) load [N], ultimate displacement [mm], and stiffness [N/mm] were recorded for each specimen. The stiffness was calculated as the slope of the best fit line to the linear part of the load-displacement curve.

A digital image correlation system (Q-400 2x12MPixel, LIMESS GmbH, Krefeld, Germany) was used to measure the full-field strains on the bone surface of CM1, with the imaging frequency set to 1 Hz. The lateral surface of the ramus bone on the implanted side was selected as the region of interest (ROI). The entire region of interest (ROI) was covered with a white paint background over which a black dot speckle pattern was applied. Two light-emitting diode (LED) panels and two digital cameras were positioned at a distance of 0.8 m from the specimen. The captured images were then processed to calculate the maximum principal strains using the software accompanying the system (*i.e.*, Istra4D x64 4.6.5, Dantec Dynamics A/S, Skovunde, Denmark).

### 1.1.3. FEA

The Abaqus/CAE 2019 (Simulia, Dassault Systèmes, France) software was used to conduct all of the FE simulations in this study. The FE model of the CM1 case was created with loads and boundary conditions that closely represented the experimental setup (Fig. 2a). INC was simulated by preventing vertical movement of the lateral and central incisors (that is, perpendicular to the plane of occlusion). The articulating surfaces of the temporomandibular joints (TMJ's) were restricted from movement in every degree of freedom. The steel loading bar was simulated as analytically rigid and non-deformable. The bar was positioned such that the distributed force could be applied similar to the experiments (Fig. 2b). A displacement of 1.5 mm was applied to the bar along the positive $z$-direction, while restricting all rotations except for the ones around the $y$-axis. The magnitude of this displacement corresponded to the linear elastic portion of the load-displacement curve obtained from the experiment. Screw fixations were modeled by applying a rigid beam constraint to the adjacent screw hole surfaces of the implant and the bone. The bar-to-bone and bone-to-bone contacts were modeled using a friction coefficient (penalty) of 0.2, and a finite sliding formulation without surface smoothing.

Four enclosed polygonal regions, denoted as Pol_1, Pol_2, Pol_3, and Pol_4, were defined at corresponding locations within ROI's of the DIC-measured and FEA-predicted strain fields (Fig. 6). The mean maximum principal strain values were obtained from each polygonal area at the yield load. The Pearson's correlation coefficient ($r$) and the standard error of estimates (*SE*) was used to evaluate the linear relationship between the computational and experimental strains.

### 1.2. Case series

The retrospective data collection for the case series was approved by

the Medical Research Ethics Committee (MEC-2022-0200) of the Erasmus MC. The inclusion criteria for the retrospective case series were as follows: patients with a benign tumor of the central or lateral mandible (edentulous or dentulous), with a segmental mandibular resection and cage implant reconstruction. The patients (>18 years old) were selected in 2022. Patients treated for malignant tumors, patients who had been or would be irradiated, and patients whose soft tissues were compromised to a large extent, were excluded from the study.

Following the inclusion criteria, three patients who had been treated at the Department of Oral and Maxillofacial Surgery of Erasmus MC were retrospectively included in the study. The first patient (hereinafter PM1) had been treated by a secondary reconstruction with a non-vascularized anterior iliac crest graft and a cage implant to recover mandibular projection (Fig. 3a-top). The primary segmental resection had been carried out for an ameloblastoma of the anterior and lateral mandible and the reconstruction had been performed with a free-vascularized osseous scapula flap. The recovery was complicated by an anterior mal-union causing a bone defect and mandibular retrognathia, necessitating the secondary reconstruction with a cage implant. The second patient (hereinafter PM2) was a primary immediate reconstruction case with a non-vascularized anterior iliac crest graft and a cage implant (Fig. 3a-middle). The anterior defect had been created after the segmental resection of a plexiform ameloblastoma. The third patient (hereinafter PM3) had had a recurrence of an earlier enucleated ameloblastoma. The resulting continuity defect on the lateral side had been reconstructed using a cage implant (Fig. 3a-bottom).

### 1.2.1. Implant design

CT scans of the head and neck region of PM1 and PM2 had been made using a Siemens SOMATOM Drive CT Scanner at 80 kVp peak potential and 0.75 mm slice thickness, while those of the head and neck region of PM3 had been made using a Siemens NAEOTOM Alpha CT Scanner at 120 kVp peak potential and 0.6 mm slice thickness. The image processing, design of the implants and surgical guides, and manufacturing were all carried out by Materialise (Leuven, Belgium). Here too, the implants were cage-shaped with design features (*i.e.*, implant thickness, clearance distance, mesh structure, and screw hole dimensions) similar to the implants used for the cadaveric cases (Fig. 3b). A non-vascularized iliac crest bone block was harvested and inserted into the cage with the intention to restore continuity and facilitate rehabilitation with dental implants. All the screw holes were planned for implant fixation with 2.0 mm self-tapping screws. The screws were placed bicortically in the mandibular segments and monocortically in the bone graft.

### 1.2.2. FEA

The Young's modulus of CP-Ti (grade 2), *E*, was assumed to be 100 GPa and was homogeneously assigned to all the implants (Barbas et al., 2012). The iliac crest bone graft was assigned with a Young's modulus of 10 GPa (Schmitz et al., 2018). The mandibular bone is a heterogeneous material consisting of cortical and cancellous bone regions with various degrees of mineralization. These local material differences could be captured through the Hounsfield units (*HU*) using CT images. The bone densities [$\rho_0$] and elastic moduli [$E$] of the bone material were calculated using the empirical equations provided by Pinheiro et al. (2021) and were assigned in Mimics Research 21.0 (Belgium) (Fig. 4a). The dentin and enamel materials were omitted in the case of CM1, as it was edentulous. The mechanical properties of all the components in the four FE models are listed in Table 1. All the components were modeled as isotropic linear elastic materials without plastic behaviors.

The mandibles (including the bone graft) and implants were discretized using 4-node tetrahedral (C3D4) elements and 10-node quadratic (C3D10) elements, respectively. The element size was determined based on a mesh convergence study. Maximum triangle edge lengths of 1 mm and 0.4 mm were used for the bone and implants,
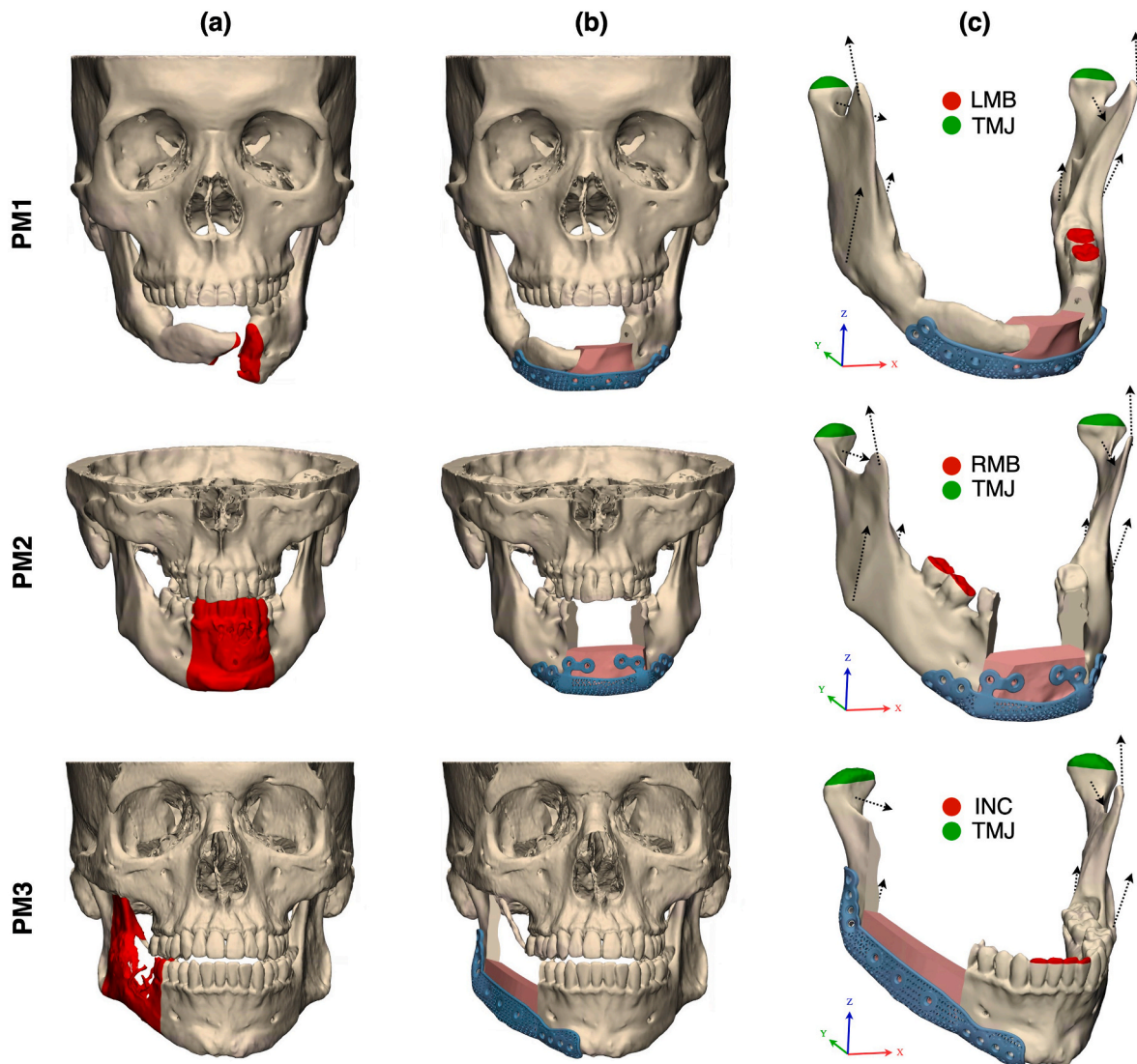
**Fig. 3.** (**a**) Mandibular resections. (**b**) Virtual planning of the reconstructions with the cage implant and iliac crest graft. (**c**) Muscle force vectors (dotted arrows) and constraints used in the FEA models. LMB = left molar biting, RMB = right molar biting, INC = incisal clenching, TMJ = temporomandibular joint.



**Fig. 4.** (**a**) A cross-section showing the volume mesh and the corresponding material assignment within the mandibular bone and molar. (**b**) The surface mesh applied to the different components. For brevity, only the PM2 case is depicted.

**Table 1**

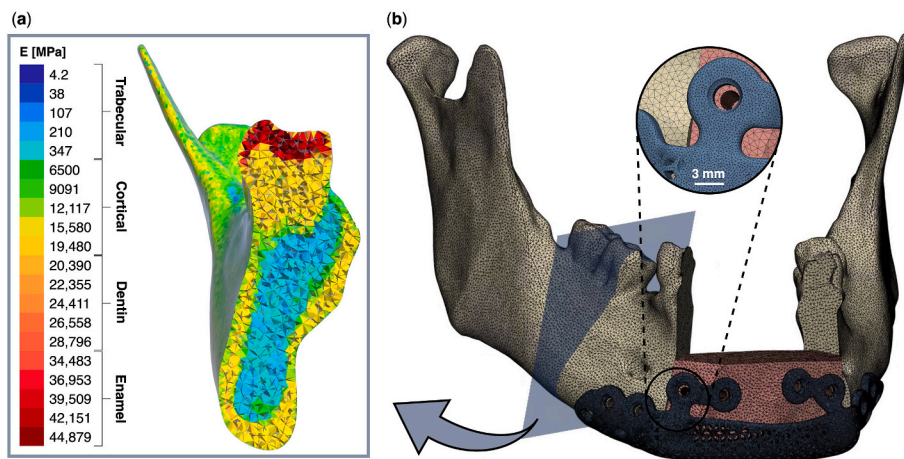The physical and mechanical properties used for the different components in the FE models. The empirical equations were adopted from Pinheiro et al. (2021).

| Tissue | CT density ($\rho_0$; [kg /m³]) | Empirical equation | Elastic modulus (E [MPa]) | Poisson's ratio ($\nu$) |
|---|---|---|---|---|
| **CM1** | | | | |
| Trabecular bone | $0 \leq \rho_0 < 1000$ | $E = 0.0004\rho_0^{2.01}$ | 4–347 | 0.30 |
| Cortical bone | $1001 \leq \rho_0 < 2000$ | $E = 0.0050\rho_0^{2.01}$ | 6500–19,486 | 0.30 |
| CP-Ti | – | – | 100,000 | 0.30 |
| **PM1-3** | | | | |
| Trabecular bone | $0 \leq \rho_0 < 1000$ | $E = 0.0004\rho_0^{2.01}$ | 4–347 | 0.30 |
| Cortical bone | $1001 \leq \rho_0 < 2000$ | $E = 0.0050\rho_0^{2.01}$ | 6500–19,486 | 0.30 |
| Dentin | $2001 \leq \rho_0 < 2480$ | $E = 0.0045\rho_0^{2.01}$ | 20,390–28,797 | 0.30 |
| Enamel | $2481 \leq \rho_0 < 2924$ | $E = 0.0050\rho_0^{2.01}$ | 34,483–44,899 | 0.30 |
| Iliac crest graft | – | – | 10,000 | 0.30 |
| CP-Ti | – | – | 100,000 | 0.30 |

respectively (Fig. 4b). A maximum triangle edge length of 0.4 mm demonstrated to preserve the geometry of the struts within the implants. At the same time, only a 6% increase of the maximum von Mises stress was measured for element sizes as small as 0.1 mm. The total numbers of the elements used for the bone and implants in each model are listed in Table 2.

The FE model of CM1 was modified to better represent the patients' clinical conditions. The loads were applied by modeling the four major muscles of mastication (*i.e.*, the masseter, temporalis, medial pterygoid, and lateral pterygoid). The directions of the muscle forces and the relative muscle force magnitudes were adopted from Korioth and Hannam (1994). The absolute values of the muscle forces were scaled using a healthy (intact) mandible model (Synbone, Model 8950, AG, Switzerland) to simulate the desired reaction forces experienced by the teeth participating in their respective clenching tasks. Even though the residual muscle force may be somewhat lower, especially at the early stages of rehabilitation, simulating full muscle forces would allow for a more conservative evaluation of the implant's safety and fixation stability. The individual muscle forces were, therefore, scaled to achieve a total reaction force that corresponded to the average maximum biting forces of 571 N and 600 N which corresponded to the values measured in healthy male individuals during incisal clenching and unilateral molar clenching, respectively (Pinheiro and Alves, 2015).

This study investigated three clenching tasks: INC, left molar biting (LMB), and right molar biting (RMB). LMB, RMB, and INC were evaluated for PM1, PM2, and PM3 respectively, based on the patients' dental situation following the reconstructive surgeries. Only INC conditions were evaluated for PM3, as the resulting stresses during LMB were expected to be lower, given its compromised musculature. The teeth involved in these clenching tasks, as well as the corresponding force vectors are presented in Fig. 3c. For the LMB and RMB tasks, the vertical motion of the occlusal surfaces of the first and second molars on their respective sides was constrained. Additionally, for the INC task, the vertical motion of the central and lateral incisors was constrained. The

**Table 2**

The total number of elements per component in the FE models.

| Model | Bone (mandible + graft) | Implant |
|---|---|---|
| CM1 | 94,940 | 133,452 |
| PM1 | 114,488 | 149,070 |
| PM2 | 101,154 | 184,238 |
| PM3 | 130,904 | 131,182 |

articulating surfaces of the TMJ were bilaterally restrained in all directions. Screw fixations were modeled as in the FE model of CM1. The scaled muscle forces for each clenching activity are summarized in Table 3. The reconstruction of PM3 resulted in a complete loss of the right masseter and right temporalis muscles, and a partial loss of the right medial pterygoid. Therefore, the loading conditions for the related FE model did not contain the right masseter and right temporalis muscles, while the right medial pterygoid muscle was modeled at 50% of the total force. In the case of PM1 and PM2, none of the aforementioned muscles were affected by the surgical procedure and were, therefore, expected to regain full muscle power.

Two stages in the rehabilitation process were simulated: (1) frictional contact with the iliac crest graft, reflecting the early post-surgical stage in which the unification of the graft with the remnant mandible had not yet been established (non-union), and (2) a "bonded" connection of the iliac crest graft with the mandibular segments (full union), assuming that the system was at a late rehabilitation stage under optimal conditions. To model the first stage, we used the same contact formulations and friction parameters for the graft and mandible contact surfaces as those utilized for CM1. In the second stage, osseointegration was assumed to have almost been completed, and loads could be transferred through the inserted graft (Shi et al., 2021; Zhong et al., 2021). The interfaces between the graft and remnant mandible were in this case modeled as bonded using tie constraints. The von Mises stresses were compared with the yield strength ($\approx$520 MPa) of the SLM CP-Ti to determine the risk of implant failure (Barbas et al., 2012).

## 2. Results

### 2.1. Cadaveric study

For both CM1 and CM2, a precise and optimal fit between the implant and the remnant mandibular segments was achieved, leading to a secure and stable screw fixation. Force-displacement graphs obtained from the quasi-static biomechanical testing of CM1 and CM2 are presented in Fig. 5a. Stiffness values of 228 N/mm and 677 N/mm were obtained for CM1 and CM2, respectively. Failure of the implant or failure at the interface between the screw and bone substrate (*e.g.*, screw loosening or screw pullout) did not occur in any of the tests. In both cases, the fracture occurred in the contralateral ramus bone at the bone-bar interface and at the ultimate loads of 470 N for CM1 and 1388 N for CM2. Cross-sections indicating the cortex thickness of the mandibular bone on the fracture side are depicted in Fig. 5b.

The FEM-predicted and DIC-measured values of the maximum principal strains corresponding to a bar displacement of 1.5 mm are presented in Fig. 6a and b, respectively. High strains were observed around the condylar neck and below the eighth screw adjacent to the resection border. Low strains were found along the posterior aspect of the ramus close to the mandibular angle and towards the coronoid process. The computationally obtained strain values were higher than the corresponding DIC-measured values by a factor of 2.7 (Fig. 6c). However, the FEA and DIC strain contour plots showed the same general distribution. A Pearson's correlation coefficient of $r = 0.92$ with standard error of estimate $SE = 29.32\,\mu\varepsilon$ was obtained from the linear fit, indicating a strong linear correlation between the DIC measurements and the FEA predictions.

### 2.2. Case series

In PM1, adjusting the harvested iliac crest to the cage required a significant amount of time. Eventually, a good fit was achieved. Post-operative bleeding had occurred, which was resolved with conservative treatment. The placement of dental implants had been possible in a second procedure and a good sagittal soft tissue profile was reached. The healing of PM2 was complicated by post-operative infection and mucosal dehiscence, resulting in prolonged nasogastric tube feeding, use

**Table 3**

The scaled muscle forces during the INC, RMB, and LMB simulated clenching tasks.

| | INC | | | RMB | | | LMB | | |
|---|---|---|---|---|---|---|---|---|---|
| | $F_x$ [N] | $F_y$ [N] | $F_z$ [N] | $F_x$ [N] | $F_y$ [N] | $F_z$ [N] | $F_x$ [N] | $F_y$ [N] | $F_z$ [N] |
| *Left lateral pterygoid* | −131.87 | −146.00 | −23.24 | −30.89 | −37.14 | −8.50 | −14.23 | −17.18 | −3.90 |
| *Left masseter* | 88.25 | −78.49 | 269.34 | 56.83 | −34.19 | 155.75 | 68.20 | −41.13 | 186.90 |
| *Left medial pterygoid* | −213.95 | −164.23 | 348.19 | −57.53 | −44.17 | 93.54 | −80.52 | −61.78 | 131.02 |
| *Left temporalis* | 12.19 | 15.78 | 60.48 | 38.44 | 60.04 | 178.40 | 45.64 | 72.89 | 211.98 |
| *Right lateral pterygoid* | 131.87 | −146.00 | −23.24 | 14.23 | −17.18 | −3.90 | 30.89 | −37.14 | −8.50 |
| *Right masseter* | −88.25 | −78.49 | 269.34 | −68.20 | −41.13 | 186.90 | −56.83 | −34.19 | 155.75 |
| *Right medial pterygoid* | 213.95 | −164.23 | 348.19 | 80.52 | −61.78 | 131.02 | 57.53 | −44.17 | 93.54 |
| *Right temporalis* | −12.19 | 15.78 | 60.48 | −45.64 | 72.89 | 211.98 | −38.44 | 60.04 | 178.40 |
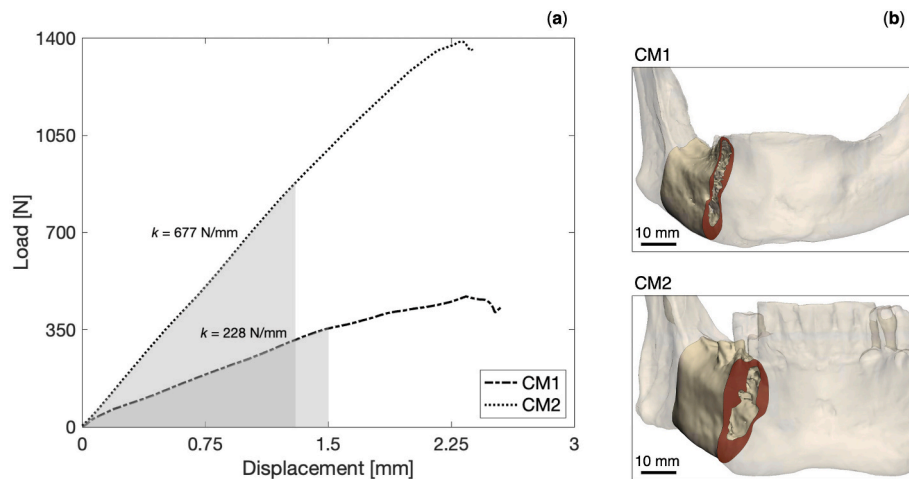


**Fig. 5.** (**a**) The experimental load-displacement curves and associated stiffness values of CM1 and CM2. The grey shaded areas indicate the linear elastic regions of the load-displacement curves. (**b**) Cross-sections in brown indicate the mandibular cortex of CM1 (top) and CM2 (bottom).
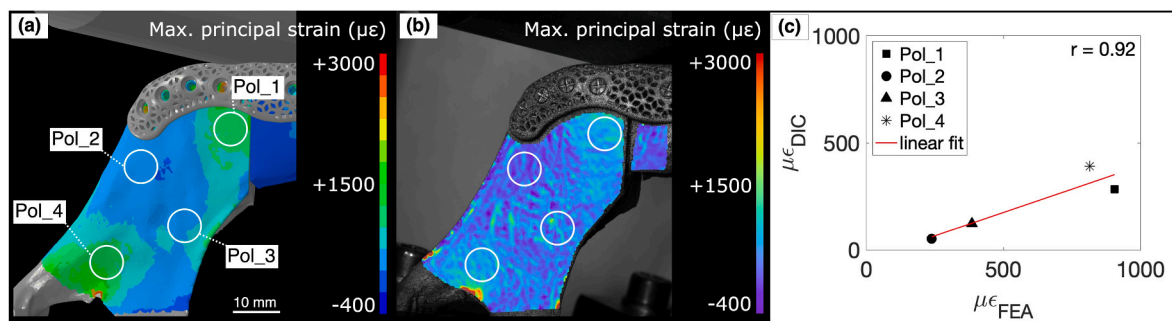


**Fig. 6.** A comparison between the (**a**) FEA-predicted and (**b**) DIC-measured maximum principal strains ($\mu\varepsilon$) on the lateral side of the ramus bone of CM1. (**c**) The DIC-measured strains ($\mu\varepsilon$) plotted against the FEA-predicted strains ($\mu\varepsilon$) obtained from the four polygonal areas as indicated in (a) and (b).

of antibiotics, and a secondary soft tissue reconstruction after the decortication of the bone graft. Although at 6 months post-operative the bone graft seemed to be partially resolved, the cage was performing its function by providing support to the chin and providing stability to both mandibular segments. Implant placement was only possible in the native proximal mandible. The graft of PM3 was readily adjusted to the cage, which was designed with slightly less caudal and lingual extension at the location of the transplant. Only a small post-operative infection occurred, which was resolved with oral antibiotics. Further healing had been uneventful, and a satisfactory mandibular contour was reached. Dental implant placement might be possible in the future.

Fig. 7 shows the von Mises stress distributions across the implant and bone components for the three patient models under non-bonded graft conditions. The peak stresses in the implants of PM1 (337 MPa) and PM3 (451 MPa) were located near the posterior screw hole closest to the

resection border. The peak stress areas of the PM2 implant (467 MPa) were also located around the screw holes closest to the edges of the resection on both sides and extended through the narrow bars that connected the main body of the implant to the screws securing the bone graft. None of the maximum stresses within the implants exceeded the yield strength of the SLM CP-Ti. For PM1 and PM2, the highest stresses in the bone were identified along the external oblique line on the contralateral side of the applied load, at the posterior and anterior sides of the condylar neck, and on the lateral side of both coronoid processes. The stresses were more equally distributed between the left and right rami in the case of PM3, with the main areas of stress concentration located around the condylar neck and along the contralateral external oblique line. Van Eijden (van Eijden, 2000) determined that the mean compressive yield strengths of cortical mandibular bone were 100 MPa, 200 MPa, and 110 MPa in the radial, longitudinal, and tangential
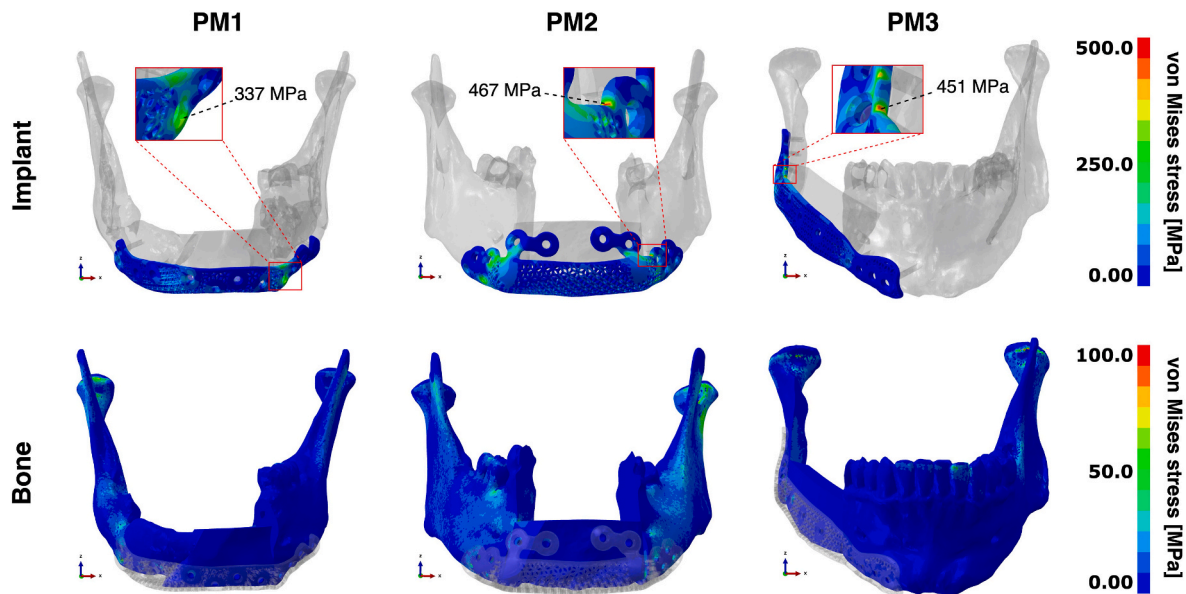
**Fig. 7.** The distribution of the von Mises stress within the implants (top) and bone (bottom) for the three patient cases under non-bonded graft conditions. The black dotted lines indicate the peak stress location on the implants.

directions, respectively. None of the peak stress areas examined showed maximum stresses exceeding these values.

Simulating the reconstructions with bonded connections between the bone graft and the remnant mandible led to a significant reduction in peak stresses within the implants. Under these conditions, the stress values within the same areas as those indicated in Fig. 7 decreased by $72.7 \pm 1.5$ % to 91 MPa, 123 MPa (right side), and 131 MPa for PM1, PM2, and PM3, respectively. The overall peak stresses, including those in the areas other than those indicated in Fig. 7, did not exceed 170 MPa in any of the three cases.

## 3. Discussion

The first objective of this study was to design cage implants for two human cadaveric mandibles with a lateral segmental defect, and to evaluate the biomechanical performance of these implants through FEA and quasi-static biomechanical testing. In the design of cage implants, topology optimization could be used. However, in this study, a fully porous implant was preferred over a topology-optimized implant. This choice was made based on the findings of a previous study conducted by our research group (van Kootwijk et al., 2022), which revealed no statistically significant differences in the mechanical performance (*i.e.*, mean stiffness, mean ultimate load, or mean ultimate displacement) between the fully porous implant and the topology-optimized implant. Additionally, the fully porous implant offered several advantages, including a lower weight, higher porosity, and notably reduced design time.

In the present study, donor profiles (*i.e.*, age and gender) of the cadaveric mandibles were not specified. However, based on the bone quality, state of dentition, and average age profile of donors, it is likely that the donors were advanced in age (Mirzaali et al., 2016). The final implant designs were additively manufactured and post-processed to match the CE-marked implants that were designed for the three patients in our case series. Implant or screw failure did not occur prior to bone fracture during quasi-static biomechanical testing, indicating that the reconstructed systems can withstand the *in-vivo* masticatory loads with a reasonable safety margin. The substantial difference in the construct stiffness between CM1 and CM2 is most likely attributable to the difference in cortex thickness (Fig. 5b), the difference in the overall bone density, and the presence of teeth, rather than to minor differences in the implant design.

Mimicking the masticatory forces in a laboratory setting is extremely challenging. The efficacy of mastication is influenced by various factors, including the presence of teeth, muscle power, malocclusion, anthropometric characteristics, such as body size and facial morphology, the extent of occlusal contact area, and other motor-related activities (Tripathi et al., 2014). Moreover, biological factors and individual healing response, which have a significant influence on the survival of the reconstruction, were not addressed in this study. In the cases of CM1 and CM2, the implants cover the mandibular angles such that the loading bar applies the forces directly to the inferior surface of the implants. *In-vivo*, however, muscle loads are not applied directly to the implant but will, instead, be transmitted from the bone through the implant. Our goal was to use a standardized test setup to obtain comparable data from the implanted constructs, despite the simplified representation of the chewing motion. Regarding cyclic tests, there were two reasons why we did not perform them in this study. First, the fatigue behavior of the materials from which this implant is made has been previously characterized (Lipinski et al., 2013). As for the implant itself, the fatigue behavior is expected to be so much dependent on the exact geometrical design, complex loading conditions, loading ratio, loading frequency, *etc.*, that such experiments are unlikely to yield generalizable or otherwise representative data. Second, performing an extensive study of the fatigue behavior of patient-specific implants is prohibitively expensive and time-consuming.

A disadvantage of CBCT is its inability to accurately display HU, since the grey density values from CBCT images are not absolute. However, studies have shown a significant relationship between *HU* in CT scans and grey scales in CBCT (Kamaruddin et al., 2016; Razi et al., 2014). Because of this and the lack of a reference imaging phantom, the material assignment for CM1 was performed in accordance with the FE models of PM1-3. The validation of the FE models representing the same experimental testing setup used in this study was carried out for synthetic mandible models in Van Kootwijk et al. (van Kootwijk et al., 2022). Therefore, conducting an extensive model validation was not the objective of this study. In contrast to the use of synthetic material and a non-implanted mandible in the previous study, this study employed real bone material and an implanted mandible in the strain analysis.

Several factors may have contributed to the disparity observed in strain values between those measured by DIC and those obtained in the FEA of CM1 (*i.e.*, with the FEA showing higher strain values by a factor of 2.7). Most importantly, a minor slippage of the steel bar down the

contralateral side (*i.e.,* posteriorly) was observed during the biomechanical testing, which was not simulated in the FEA. Because of this, a slightly lower force may have been exerted on the implanted side for an equal *z*-displacement of the bar, resulting in lower strains detected by the DIC system as compared to the FEA. Besides, the FE model is based on simplified assumptions about the material behavior, such as isotropy and linear elasticity, whereas the bone shows anisotropic and viscoelastic behavior. Moreover, the process of calculating strains in a correlation algorithm involves the use of grids with finite sizes. The strain values calculated for such a grid is the average strain of individual points within the area covered by an individual cell within the grid. Such an averaging step, which is inherent to the DIC method, tends to reduce peak strain values as compared to FEA where strain values are calculated for each integration point. Finally, a relatively thick paint coating had to be applied to the ROI to increase the contrast and to increase the adhesion of the paint to the rough and irregular bone surface. In DIC, the application of multiple thin paint layers is preferred to a single thick layer, as a thin and well-adhering layer of paint ensures that the deformation of the speckle pattern more closely corresponds to the deformation of the bone. Therefore, the thicker paint coating may have led to a slight underestimation of strain. Despite the discrepancies in strain magnitude between the FEA and DIC strain contour plots, their general distribution displays a strong linear correlation, supporting the validity of the analysis.

The second objective of this study was to evaluate cage implants of comparable designs under post-operative conditions with validated FE methods. The three patient cases included in this study were the first to receive treatments with patient-specific cage implants within the Department of Oral and Maxillofacial Surgery, Erasmus MC. Due to the relative novelty of this technique, not only within our department but also in other medical facilities, there is limited literature available for comparison with similar reconstructions, making it difficult to fully evaluate the various aspects of this technique. For example, detailed descriptions of the surgical procedures involved, as well as long-term clinical outcomes were beyond the scope of this study. Long-term patient follow-ups are, however, required to quantify bony ingrowth, evaluate the bony union of the inserted graft at the osteotomy sites, and assess the feasibility of dental rehabilitation, which is valuable when comparing clinical outcomes with computational predictions. In the event of any mechanical failures of the osteosynthesis, one can compare the primary sites of implant failure observed clinically with the regions that correspond to the elevated von Mises stresses as predicted by the FE models. As the use of cage reconstructions continues to grow, the number of patients available for retrospective studies gradually increases. This will make it possible to conduct larger case series studies and to include long-term functional outcomes and comparisons between different materials and surgical techniques.

The maximum bite force of healthy adults with full dentition varies from person to person. The chewing forces are typically reduced after (partial) resection of the mandible. The amount of reduction may be difficult to predict on an individual basis, as this greatly depends on the type of defect, the degree of muscle preservation, the method of reconstruction, and the course of recovery. Maurer et al. (2006) found an average reduction of 76% in bite force in the molar region and 59% in the incisor region. In this study, the patients' FE models were subjected to bite forces corresponding to the average maximum bite strength for a healthy individual to simulate a worst-case scenario. None of the three implant designs from the case series experienced implant stresses that exceeded the yield strength of SLM CP-Ti when simulated under highly strenuous chewing conditions and with a non-unified bone graft. Simulating a full union between the graft and remnant mandible substantially reduced the peak stresses within the implants. With reference to the findings from the study conducted by Hedayati et al. (2017), it is expected that both the static and fatigue properties of the implants will improve over time as bone continues to grow into them. Given these insights, it becomes essential to establish an optimal environment for bone integration, as it can impact the long-term durability of the implants.

In this study, we focused on the development and evaluation of cage implants as a suitable alternative to conventional free-flap reconstructions. However, the clinical use of this type of implants is limited to a small patient population and imposes potential risks, including infection, wound dehiscence, bone resorption, and intra-oral exposure of the implant, which may lead to (partial) loss of the bone graft or implant. Nevertheless, the techniques proposed in this study are not limited to cage implants and can, in principle, be applied for the development of patient-specific reconstruction plates, miniplates, or other alloplastic solutions.

## 4. Conclusions

We performed a cadaveric study as well as a retrospective case series study to evaluate the performance of patient-specific 3D printed mandibular implants. The cadaveric study has shown that the digital workflow proposed is effective in designing cage implants for mandibles with varied morphologies and with satisfactory mechanical functioning under demanding chewing conditions. The FEA results of the case series demonstrated that all the cage implants could resist the masticatory loads at the level of the maximum bite force observed in healthy adults. However, more research is needed to thoroughly evaluate the osteogenic potential of bone graft insertions. Even though the implants appear to be capable of resisting the masticatory forces independently, a rebuild continuity of the bone would improve the load distribution within the construct and increases the likelihood of subsequent rehabilitation with dental implants. Given the load-bearing nature of this type of cage implants, we highly recommend the use of FEA in pre-surgical planning for predicting construct stresses at various post-implantation stages and to optimize the design of the implants and their associated fixation mechanisms.

**Ethical approval**

This scientific research does not fall under the Medical Research Involving Human Subjects Act (WMO) as confirmed by the Medical Research Ethics Committee of the Erasmus MC (MEC-2022-0200).

**CRediT authorship contribution statement**

**A. van Kootwijk:** Writing – original draft, Visualization, Validation, Software, Methodology, Investigation, Formal analysis, Data curation, Conceptualization. **B.P. Jonker:** Writing – review & editing, Resources, Methodology, Investigation, Conceptualization. **E.B. Wolvius:** Writing – review & editing, Resources, Methodology, Conceptualization. **M. Cruz Saldivar:** Investigation. **M.A. Leeflang:** Investigation. **J. Zhou:** Writing – review & editing, Conceptualization. **N. Tümer:** Writing – review & editing, Methodology, Conceptualization. **M.J. Mirzaali:** Writing – review & editing, Project administration, Methodology, Conceptualization. **A.A. Zadpoor:** Writing – review & editing, Project administration, Funding acquisition.

**Declaration of competing interest**

The authors declare that they have no known competing financial interests or personal relationships that could have appeared to influence the work reported in this paper.

**Data availability**

The authors do not have permission to share data.

## Acknowledgements

## Appendix A. Supplementary data

Supplementary data to this article can be found online at https://doi.org/10.1016/j.jmbbm.2023.106097.

## References

Azarniya, A., Colera, X.G., Mirzaali, M.J., Sovizi, S., Bartolomeu, F., St Weglowski k, M., Wits, W.W., Yap, C.Y., Ahn, J., Miranda, G., Silva, F.S., Madaah Hosseini, H.R., Ramakrishna, S., Zadpoor, A.A., 2019. Additive manufacturing of Ti–6Al–4V parts through laser metal deposition (LMD): process, microstructure, and mechanical properties. J. Alloys Compd. 804, 163–191. https://doi.org/10.1016/j.jallcom.2019.04.255.

Barbas, A., Bonnet, A.-S., Lipinski, P., Pesci, R., Dubois, G., 2012. Development and mechanical characterization of porous titanium bone substitutes. J. Mech. Behav. Biomed. Mater. 9, 34–44.

Gateno, J., Cookston, C., Hsu, S.S.-P., Stal, D.N., Durrani, S.K., Gold, J., Ismaily, S., Alexander, J.W., Noble, P.C., Xia, J.J., 2013. Biomechanical evaluation of a new MatrixMandible plating system on cadaver mandibles. J. Oral Maxillofac. Surg. 71, 1900–1914. https://doi.org/10.1016/j.joms.2013.06.218.

Hedayati, R., Janbaz, S., Sadighi, M., Mohammadi-Aghdam, M., Zadpoor, A.A., 2017. How does tissue regeneration influence the mechanical behavior of additively manufactured porous biomaterials? J. Mech. Behav. Biomed. Mater. 65, 831–841.

Kakarala, K., Shnayder, Y., Tsue, T.T., Girod, D.A., 2018. Mandibular reconstruction. Oral Oncol. 77, 111–117. https://doi.org/10.1016/j.oraloncology.2017.12.020.

Kamaruddin, N., Rajion, Z.A., Yusof, A., Aziz, M.E., 2016. Relationship between Hounsfield unit in CT scan and gray scale in CBCT. In: AIP Conf Proc. AIP Publishing.

Kondo, S., Katsuta, H., Akizuki, A., Kurihara, Y., Kamatani, T., Yaso, A., Nagasaki, M., Shimane, T., Shirota, T., 2015. Computer-assisted surgery for mandibular reconstruction using a patient-specific titanium mesh tray and particulate cancellous bone and marrow. Case Rep. Clin. Med. 4, 85–92. https://doi.org/10.4236/crcm.2015.43019.

Korioth, T.W.P., Hannam, A.G., 1994. Deformation of the human mandible during simulated tooth clenching. J. Dent. Res. 73, 56–66.

Kumar, B.P., Venkatesh, V., Kumar, K.A., Yadav, B.Y., Mohan, S.R., 2016. Mandibular reconstruction: overview. J. Maxillofac. Oral Surg. 15, 425–441 (n.d.).

Lee, W.-B., Choi, W.-H., Lee, H.-G., Choi, N.-R., Hwang, D.-S., Kim, U.-K., 2018. Mandibular reconstruction with a ready-made type and a custom-made type titanium mesh after mandibular resection in patients with oral cancer. Maxillofac Plast Reconstr Surg 40, 35. https://doi.org/10.1186/s40902-018-0175-z.

Lipinski, P., Barbas, A., Bonnet, A.-S., 2013. Fatigue behavior of thin-walled grade 2 titanium samples processed by selective laser melting. Application to life prediction of porous titanium implants. J. Mech. Behav. Biomed. Mater. 28, 274–290.

Louvrier, A., Marty, P., Barrabé, A., Euvrard, E., Chatelain, B., Weber, E., Meyer, C., 2017. How useful is 3D printing in maxillofacial surgery? J Stomatol Oral Maxillofac Surg 118, 206–212. https://doi.org/10.1016/j.jormas.2017.07.002.

Malekpour, Z., Sarkarat, F., Hooshangi, H., 2014. Mandibular reconstruction using custom-made titanium mesh tray and autogenous bone graft- A case report. Thrita 3. https://doi.org/10.5812/thrita.22291.

Maurer, P., Pistner, H., Schubert, J., 2006. Computergestützte Kaukraftanalyse bei Patienten mit Unterkieferkontinuitätsresektionen. Oral Maxillofac. Surg. 10, 37.

Mirzaali, M.J., Schwiedrzik, J.J., Thaiwichai, S., Best, J.P., Michler, J., Zysset, P.K., Wolfram, U., 2016. Mechanical properties of cortical bone and their relationships with age, gender, composition and microindentation properties in the elderly. Bone 93, 196–211.

Mirzaali, M.J., Moosabeiki, V., Rajaai, S.M., Zhou, J., Zadpoor, A.A., 2022. Additive manufacturing of biomaterials-design principles and their implementation. Materials 15, 5457. https://doi.org/10.3390/ma15155457.

Mirzaali, M.J., Shahriari, N., Zhou, J., Zadpoor, A.A., 2023. Quality of AM implants in biomedical application. In: Quality Analysis of Additively Manufactured Metals. Elsevier, pp. 689–743. https://doi.org/10.1016/B978-0-323-88664-2.00015-4.

Oldhoff, M.G.E., Mirzaali, M.J., Tümer, N., Zhou, J., Zadpoor, A.A., 2021. Comparison in clinical performance of surgical guides for mandibular surgery and temporomandibular joint implants fabricated by additive manufacturing techniques. J. Mech. Behav. Biomed. Mater. 119, 104512 https://doi.org/10.1016/j.jmbbm.2021.104512.

Paré, A., Bossard, A., Laure, B., Weiss, P., Gauthier, O., Corre, P., 2019. Reconstruction of segmental mandibular defects: current procedures and perspectives. Laryngoscope Investig Otolaryngol 4, 587–596. https://doi.org/10.1002/lio2.325.

Pinheiro, M., Alves, J.L., 2015. The feasibility of a custom-made endoprosthesis in mandibular reconstruction: implant design and finite element analysis. J. Cranio-Maxillofacial Surg. 43, 2116–2128.

Pinheiro, M., Willaert, R., Khan, A., Krairi, A., Van Paepegem, W., 2021. Biomechanical evaluation of the human mandible after temporomandibular joint replacement under different biting conditions. Sci. Rep. 11, 14034.

Rachmiel, A., Shilo, D., Blanc, O., Emodi, O., 2017. Reconstruction of complex mandibular defects using integrated dental custom-made titanium implants. Br. J. Oral Maxillofac. Surg. 55, 425–427. https://doi.org/10.1016/j.bjoms.2017.01.006.

Razi, T., Niknami, M., Ghazani, F.A., 2014. Relationship between Hounsfield unit in CT scan and gray scale in CBCT. J. Dent. Res. Dent. Clin. Dent. Prospects 8, 107.

Schmitz, P., Cornelius Neumann, C., Neumann, C., Nerlich, M., Dendorfer, S., 2018. Biomechanical analysis of iliac crest loading following cortico-cancellous bone harvesting. J. Orthop. Surg. Res. 13, 1–8.

Schupp, W., Arzdorf, M., Linke, B., Gutwald, R., 2007. Biomechanical testing of different osteosynthesis systems for segmental resection of the mandible. J. Oral Maxillofac. Surg. 65, 924–930. https://doi.org/10.1016/j.joms.2006.06.306.

Shi, Q., Sun, Y., Yang, S., Van Dessel, J., Lübbers, H.-T., Zhong, S., Gu, Y., Bila, M., Politis, C., 2021. Preclinical study of additive manufactured plates with shortened lengths for complete mandible reconstruction: design, biomechanics simulation, and fixation stability assessment. Comput. Biol. Med. 139, 105008.

Tripathi, G., Ponnanna, A.A., Rajwadha, N., Chhaparia, N., Sharma, A., Anant, M., 2014. Comparative evaluation of maximum bite force in dentulous and edentulous individuals with different facial forms. J. Clin. Diagn. Res. 8, ZC37.

van Eijden, T., 2000. Biomechanics of the mandible. Crit. Rev. Oral Biol. Med. 11, 123–136.

van Kootwijk, A., Moosabeiki, V., Saldivar, M.C., Pahlavani, H., Leeflang, M.A., Kazemivand Niar, S., Pellikaan, P., Jonker, B.P., Ahmadi, S.M., Wolvius, E.B., Tümer, N., Mirzaali, M.J., Zhou, J., Zadpoor, A.A., 2022. Semi-automated digital workflow to design and evaluate patient-specific mandibular reconstruction implants. J. Mech. Behav. Biomed. Mater. 132, 105291 https://doi.org/10.1016/j.jmbbm.2022.105291.

Yamashita, Y., Yamaguchi, Y., Tsuji, M., Shigematsu, M., Goto, M., 2008. Mandibular reconstruction using autologous iliac bone and titanium mesh reinforced by laser welding for implant placement. Int. J. Oral Maxillofac. Implants 23, 1143–1146.

Zhong, S., Shi, Q., Sun, Y., Yang, S., Van Dessel, J., Gu, Y., Chen, X., Lübbers, H.-T., Politis, C., 2021. Biomechanical comparison of locking and non-locking patient-specific mandibular reconstruction plate using finite element analysis. J. Mech. Behav. Biomed. Mater. 124, 104849.

Zhou, L., Shang, H., He, L., Bo, B., Liu, G., Liu, Y., Zhao, J., 2010. Accurate reconstruction of discontinuous mandible using a reverse engineering/computer-aided design/rapid prototyping technique: a preliminary clinical study. J. Oral Maxillofac. Surg. 68, 2115–2121. https://doi.org/10.1016/j.joms.2009.09.033.